Dynamics of microswimmers near a liquid-liquid interface with viscosity difference

Chao Feng, John J. Molina, and Ryoichi Yamamoto
Department of Chemical Engineering, Kyoto University, Kyoto 615-8510, Japan
Matthew S. Turner
Department of Chemical Engineering, Kyoto University, Kyoto 615-8510, Japan and
Department of Physics, University of Warwick, Coventry CV4 7AL, UK

(*Electronic mail: ryoichi@cheme.kyoto-u.ac.jp)

(Dated: 12 June 2023)

Transport of material across liquid interfaces is ubiquitous for living cells and is also a crucial step in drug delivery and in many industrial processes. The fluids that are present on either side of the interfaces will usually have different viscosities. We present a physical model for the dynamics of microswimmers near a soft and penetrable interface that we solve using computer simulations of Navier-Stokes flows. The literature contains studies of similar isoviscous fluid systems, where the two fluids have the same viscosity. Here we extend this to the more general case where they have different viscosities. In particular, we investigate the dynamics of swimmers approaching a fluid-fluid interface between phase-separated fluids with distinct viscosities. We find that the incoming angle, viscosity ratio, and swimming type (i.e., pusher, puller, or neutral) strongly influence the collision, resulting in four distinct dynamical modes: bouncing, sliding, penetrating, and hovering. The former three modes are also observed for isoviscous systems, while the hovering, in which strong pullers swim parallel to the interface at a non-zero distance, requires mismatched viscosities. Furthermore, swimmers exhibit a preference for lower-viscosity fluids, known as viscotaxis. This implies that, for a wide distribution of contact angles, more swimmers will transition into the low-viscosity environment than vice versa. Consequently, a swimmer starting in a low-viscosity fluid is more likely to bounce back at the interface, while a swimmer in a high-viscosity fluid is more likely to penetrate the interface and enter the lower-viscosity fluid.

I. INTRODUCTION

Across the natural world, it is common for microswimmers to navigate through complex fluid environments, e.g., spermatozoa in seminal plasma and cervical mucus[1–3]. Transmembrane transport of bacteria and viruses is also a key stage in infection.[4] Therefore, research into the dynamics of swimmers in such environments is of vital importance to understand many biological transport processes, as well as for the development of potential future artificial micro-machines, which could be used for targeted delivery in complex fluid environments.[5–9]

Most studies on the dynamics of microswimmers in inhomogeneous multi-phase systems have focused on swimming in the vicinity of boundaries, mainly solid-fluid boundaries[10–19] and fluid-air interfaces[10,20], or have been restricted to simplified 2D systems[21–23]. For example, Lauga *et al.*[17] showed that E. coli was shown to exhibit a clockwise circular swimming motion near a solid-fluid boundary, whereas Leonardo *et al.*[20] report a counterclockwise rotation near a free surface, such as the fluid-air interface. In both cases, this circular motion can be explained as arising from the hydrodynamic interactions.

However, few theoretical studies have attempted to construct a general hydrodynamic description of microswimmers near (complex) fluid-fluid interfaces[18,24–26] , i.e., near the boundaries between immiscible fluids. This may be due to the high computational costs associated with treating deformable and penetrable boundaries. Of particular (biological) importance is the case where fluids have mismatched viscosities. This can dramatically affect the swimmer dynamics. For example, spermatozoa exhibit very different tail waveforms, depending on the viscosity of the fluid[1,27]. Sperm in low viscosity medium has a significant side-to-side movement across the directional axis. However, in high-viscosity fluids, e.g., mucus, such head yaw is reduced by using a distinct "meandering" waveform with less lateral movement across the directional axis. In this way, the spermatozoa are able to swim with approximately the same velocity in either fluid, saline or mucus, despite the large viscosity difference between the two.

Previously, we have studied the dynamics of microswimmers near a soft, deformable and penetrable interface in an isoviscous system[28]. In this paper, we extend our work to consider the dynamics of swimmers at the interface of two fluids with mismatched viscosities. First, we review the computational model we have used, and detail how it is extended to take the variable viscosity into account. Then, we analyse the effect of the viscosity on the motion of the swimmer in the low Reynolds-number regime. As we previously found for the isoviscous case, different initial trajectories can lead to motion that we characterise as "bouncing", "sliding", and "penetrating". In addition to these modes, we also observe a new dynamical "hovering" mode, in which the swimmer tends to move parallel to the interface, at a fixed (non-zero) distance. By analysing the time evolution of the positions and orientations, we found several sets of trajectories for the bouncing and penetrating motions that exhibit time-reversal symmetry due to the pushers/puller duality. Compared to the isoviscous case, we find that a viscosity difference can significantly affect the dynamics during a collision with the interface, i.e., the relationship between incoming and outgoing angles. Finally, we provide an analysis of the swimmer dynamics in the hovering motion. Interestingly, both the trajectories and the time evolution of the orientation are similar to those of swimmers near a solid wall.

II. SIMULATION METHODS

A. The squirmer model

We model swimmers as spherical squirmers, one of the most widely employed mathematical models for microswimmers, originally developed to describe the motion of ciliated micro-organism (e.g., Paramecium) that propel themselves through the synchronized beating of cilia at their surface[29,30]. Thus, swimmers are represented as rigid spherical particles, with a modified stick boundary condition at their surface, which drives the flow and is responsible for the propulsion, as shown in Fig. 1(b). Since the swimmer is modelled as a perfectly rigid sphere, with no chirality, only tangential components of the surface slip velocity are considered, i.e., all azimuthal and radial modes are set to zero[31,32]. These neglected modes would be required, for example, to model the beating of the envelope of flagella at the surface of a Volvox colony with swirl[33]. The surface slip velocity is given as

$$\boldsymbol{u}^s(\vartheta) = \sum_{n=1}^{\infty} \frac{2}{n(n+1)} B_n P_n^{'}(\cos\vartheta)\sin\vartheta\hat{\boldsymbol{\vartheta}}, \tag{1}$$

where $\vartheta = \cos^{-1}(\hat{\boldsymbol{r}}\cdot\hat{\boldsymbol{e}})$ is the polar angle between the swimming direction $\hat{\boldsymbol{e}}$ and $\hat{\boldsymbol{r}}$, a unit vector directed from the centre of the squirmer toward the corresponding point on its surface and $\hat{\boldsymbol{\vartheta}}$ is the unit vector orthogonal to $\hat{\boldsymbol{r}}$. $P_n^{'}$ is the derivative of the Legendre polynomial of the n-th order, and B_n is the magnitude of each mode. We note that this tangential approximation refers only to the slip velocity imposed at the particle surface in order to generate the self-propulsion (i.e., a modified stick-boundary condition). No constraints are imposed on the total fluid velocity field.

Only the first two terms are included, B_1 and B_2, in the tangential slip velocity to concentrate on the fundamental hydrodynamic effects. These two terms, which decrease as $1/r^2$ and $1/r^3$, respectively, govern the swimming velocity and the stresslet. Higher-order contributions which decrease more rapidly have been disregarded since they do not provide any insight into the differences between pusher and puller dynamics.

$$\boldsymbol{u}^s(\vartheta) = B_1(\sin\vartheta + \frac{\beta}{2}\sin 2\vartheta)\hat{\boldsymbol{\vartheta}}, \tag{2}$$

The coefficient of the first term in Eq. 2, B_1, determines the steady-state swimming velocity of the squirmer $U_0 = 2/3B_1$. The coefficient of the second mode, B_2, determines the stress exerted by the particles on the fluid. The ratio $\beta = B_2/B_1$ determines the swimming type and strength. When β is negative, the squirmer is a pusher, which swims generating an extensile flow field (e.g., *E. coli*); when β is positive, the squirmer is a puller, which swims generating a contractile flow field (e.g., *C. reinhardtii*). The marginal case of $\beta = 0$ corresponds to a neutral particle, which is accompanied by a potential flow (e.g., *Volvox*). In what follows, we will refer to squirmers with $|\beta| \leq 1$ as being weak, and those with $|\beta| \geq 4$ as being strong.

B. Smoothed profile method for binary fluids

To simulate the dynamics of particles dispersed in an immiscible binary A/B fluid system, while fully accounting for the hydrodynamic interactions, we consider the coupled equations of motion for the solid particles and the component fluids within the model-H representation, i.e., the Newton-Euler and Cahn-Hilliard Navier-Stokes equations[34–36]. Furthermore, to allow for efficient calculations of many-particle systems, while still providing an accurate description of the many-body hydrodynamic interactions, we employ the Smooth Profile (SP) method[37]. Within this approximation, the sharp particle boundaries are replaced by diffuse interfaces of finite thickness. The solid particle domains are thus defined using a continuous order parameter or phase-field ϕ, defined over the whole computational domain. The A/B fluid phases are likewise defined in terms of the corresponding A/B order parameters ψ_A and ψ_B. This allows us to easily couple the rigid-body dynamics to the dynamics of the (phase-separating) fluids. In what follows we briefly describe how to solve for the (coupled) rigid-body dynamics, phase-separating dynamics, and fluid dynamics.

Detailed descriptions of the SP method and its implementation and can be found in our earlier publications[37,38]. We note that reasonable accuracy at reduced computational cost can be obtained even when using relatively coarse resolutions, i.e., particles of radius $a = 4 \sim 5\Delta$, with interfacial thickness $\xi = 2\Delta$ (Δ the grid spacing). For example, the drag coefficient of infinitely long cylindrical rods (2D) is within $\lesssim 5\%$ of the analytical solutions to the Stokes equation[39]. A similar level of agreement is obtained for the (3D) friction and mobility tensors of non-spherical particle assemblies[40]. The SP method has been used to study the electrophoresis[41], sedimentation[42], and rheology of colloidal suspesions[43], as well as the attachment of particles to bubble surfaces[35], the capillary-induced bending of flexible fibres[36], and the enhanced diffusion of swimming particles[44], among others. For the specific case of squirmers at fluid-fluid interfaces considered here, our previous results for isoviscous systems[28] are in good quantitative agreement with the Lattice-Boltzmann simulations of Gidituri et al.[26], who studied the reorientation dynamics of squirmers trapped at the interface. Whenever comparison with experiments, analytical results, or alternative simulations, has been possible, SP results have shown excellent agreement ($\lesssim 5-10\%$). A detailed error analysis of the SP method, with comparisons to direct numerical simulations and the force coupling method, has been performed by Luo et al.[45].

1. *Particle Dynamics*

The rigid particle dynamics are determined by Newton–Euler equations of motion (assuming spherical particles):

$$\dot{\boldsymbol{R}}_i = \boldsymbol{V}_i, \tag{3}$$

$$\dot{\boldsymbol{Q}}_i = \mathrm{skew}(\boldsymbol{\Omega}_i) \cdot \boldsymbol{Q}_i, \tag{4}$$

$$M_i \dot{\boldsymbol{V}}_i = \boldsymbol{F}_i^H + \boldsymbol{F}_i^C + \boldsymbol{F}_i^{ext}, \tag{5}$$

$$\boldsymbol{I}_i \cdot \dot{\boldsymbol{\Omega}}_i = \boldsymbol{N}_i^H + \boldsymbol{N}_i^{ext}, \tag{6}$$

where $\boldsymbol{R}_i$, $\boldsymbol{Q}_i$, $\boldsymbol{V}_i$, $\boldsymbol{\Omega}_i$ are the positions, orientation matrices, velocities, and angular velocities of particle i, respectively; M_i are the masses, and $\boldsymbol{I}_i = 2/5 M_i {a_i}^2 \mathsf{I}$ the moments of inertia for spheres of radius a_i (I the unit tensor); $\mathrm{skew}(\boldsymbol{\Omega}_i)$ is the skew-symmetric matrix for the angular velocity. The hydrodynamic forces and torques are given by $\boldsymbol{F}_i^H$ and $\boldsymbol{N}_i^H$. In this work, we only consider the dynamics of a single particle, so there is no direct particle-particle interaction $\boldsymbol{F}_i^c = \boldsymbol{N}_i^c = 0$. $\boldsymbol{F}_i^{ext}$ and $\boldsymbol{N}_i^{ext}$ are the external forces and torques, respectively, and are equal to 0 since the swimmers are buoyancy-neutral particles.

Within the SP method, the particle domain is accounted for by an order parameter $\phi(\boldsymbol{r})$, which can be interpreted as the volume fraction of the solid component in the system

$$\phi(\boldsymbol{r}) = \sum_i \phi_i(\boldsymbol{r}), \tag{7}$$

where ϕ_i is the phase-field for particle i. This particle phase field is defined such that it is equal to 1 in the solid domain, 0 in the fluid domain, and smoothly interpolates between the two domains across the interfaces (of width ξ_p). In this way, the boundaries can be represented through the gradient of the phase field. We can then define the velocity field for the particle domain as

$$\phi \boldsymbol{u}_p = \sum_i \phi_i [\boldsymbol{V}_i + \boldsymbol{\Omega}_i \times \boldsymbol{R}_i]. \tag{8}$$

2. *Phase-Separating Dynamics*

The order parameters for the A and B phases, $\psi_A(\boldsymbol{r})$ and $\psi_B(\boldsymbol{r})$, represent the volume fractions of the constituent components ($0 \leq \phi_\alpha \leq 1$). Furthermore, since the sum total of the volume fraction of all components (fluids and particles) is constrained to be unity,

$$\psi_A + \psi_B + \phi = 1, \tag{9}$$

the composition of the A/B phase-separating fluid can be described in terms of a single order parameter $\psi(\boldsymbol{r})$,

$$\psi = \psi_A - \psi_B. \tag{10}$$

This order parameter $\psi(\boldsymbol{r})$ is defined to be equal to 1 in the A domain and -1 in the B domain.

The dynamics for $\psi(\boldsymbol{r})$ is determined by the following modified Cahn-Hilliard equation

$$\frac{\partial \psi}{\partial t} + (\boldsymbol{u} \cdot \boldsymbol{\nabla})\psi = \kappa \nabla^2 \mu_\psi, \tag{11}$$

where $\boldsymbol{u}$ is the total velocity field, κ is the mobility coefficient, and $\mu_\psi = \delta \mathscr{F} / \delta \psi$ is the chemical potential associated with the order parameter ψ. In what follows we will also need to account for the fluid-particle interactions using a sec-

TABLE I: Symbols and Abbreviations

	Squirmer Model
B_n	coefficient of n tangential squirming mode
$P_n^{'}$	derivative of the n-order Legendre polynomial
$\hat{\boldsymbol{u}}^s$	surface slip velocity field
β	swimming type ($\beta = B_2/B_1$)
$\hat{\boldsymbol{e}}$	swimming direction
θ	swimming direction angle
U	(steady-state) swimming velocity ($U = 2/3B_1$)
	Rigid Particle Model
a	radius
$\boldsymbol{R}$	position
$\boldsymbol{Q}$	orientation matrix
$\boldsymbol{V}$	velocity
$\boldsymbol{\Omega}$	angular velocity
$\boldsymbol{F}^C$ $(\boldsymbol{N}^C)$	direct particle-particle interaction force (torque)
$\boldsymbol{F}^{ext}(\boldsymbol{N}^{ext})$	external force (torque)
$\boldsymbol{F}^H$ $(\boldsymbol{N}^H)$	hydrodynamic force (torque)
$\boldsymbol{I}$	moment of inertia
$\boldsymbol{J}$	angular momentum
M	mass
$\hat{\boldsymbol{v}}$	direction of motion
φ	direction of motion angle
	Fluid Model
p	pressure
$\boldsymbol{\sigma}$	Newtonian stress tensor
$\boldsymbol{u}$	total velocity field
$\boldsymbol{u}_f$	fluid velocity field
$\boldsymbol{u}_p$	particle velocity field
ρ	density
ρ_i	fluid density ($i = A, B$)
ρ_p	particle density
η	total viscosity
η_i	fluid viscosity ($i = A, B$)
η_p	particle viscosity
λ	viscosity ratio ($\lambda = \eta_B/\eta_A$)
ϕ	particle phase field function
ξ_p	particle–fluid interface thickness
	Phase Separation Model
ψ_i	fluid phase field function ($i = A, B$)
ψ	binary fluid phase field function ($\psi = \psi_A - \psi_B$)
μ_γ	chemical potential of γ order parameter ($\gamma = \psi, \phi$)
ξ_f	fluid-fluid interfacial thickness
w	particles' affinity to A/B fluid phases
α	A/B interfacial tension coefficient
κ	mobility coefficient for ψ field
	System Parameters
l_x, l_y, l_z	system width, length, height
Δ	grid spacing/unit of length
	Abbreviations & Acronyms
DNS	direct numerical simulations
Pe	Péclet number
Re	Reynolds number
Sc	Schmidt number
SP	Smoothed Profile

ond chemical potential associated with the ϕ order parameter, $\mu_\phi = \delta\mathscr{F}/\delta\phi$. These chemical potentials are derived from the Ginzburg-Landau free energy functional

$$\mathscr{F}[\psi,\phi] = \frac{k_B T}{v_0}\int \mathrm{d}\boldsymbol{r}\left[f(\psi) + \frac{\alpha}{2}(\boldsymbol{\nabla}\psi)^2 + w\xi_p\psi(\boldsymbol{\nabla}\phi)^2\right] \tag{12}$$

where k_B is the Boltzmann constant, T the temperature, and v_0 a reference unit volume. The first term in the integrand of Eq. 12, $f(\psi) = \frac{1}{4}\psi^4 - \frac{1}{2}\psi^2$ represents the Landau double-well potential, with two minima at $\psi = 1$ and -1. The potential energy associated with the A/B interface is represented by the second term, which corresponds to the surface tension of the interface. The third term represents the particles' affinity for each of the fluid A/B phases. Additional terms can be added to model more elaborate chemical interactions, e.g., particle affinity to interface, but are not considered in this work. The chemical potentials corresponding to this free-energy functional are then

$$\mu_\psi = \frac{k_B T}{v_0}\left[f'(\psi) + \alpha\nabla^2\psi + w\xi_p(\boldsymbol{\nabla}\phi)^2\right] \tag{13}$$

$$\mu_\phi = \frac{k_B T}{v_0}\left[2w\xi_p(\boldsymbol{\nabla}\psi\cdot\boldsymbol{\nabla}\phi + \psi\nabla^2\phi)\right]. \tag{14}$$

In what follows we assume that the particles will interact with the interface hydrodynamically but not chemically and so we set $w = 0$ in all the simulations reported below.

3. *Fluid dynamics*

The total velocity, which accounts for both the fluid and particle domains, is defined as

$$\boldsymbol{u} = (1-\phi)\boldsymbol{u}_f + \phi\boldsymbol{u}_p, \tag{15}$$

where the first term gives the fluid velocity field and the second term the particle velocity field. Then, the time evolution of this total flow field $\boldsymbol{u}$ is given by a modified version of the Navier-Stokes and continuity equations

$$\begin{aligned}\rho(\partial_t + \boldsymbol{u}\cdot\boldsymbol{\nabla})\boldsymbol{u} &= \boldsymbol{\nabla}\cdot\boldsymbol{\sigma} + \rho(\phi\boldsymbol{f}_p + \boldsymbol{f}_{sq}) \qquad (16)\\ &\quad - \psi\boldsymbol{\nabla}\mu_\psi - \phi\boldsymbol{\nabla}\mu_\phi,\\ \boldsymbol{\nabla}\cdot\boldsymbol{u} &= 0 \qquad (17)\end{aligned}$$

where $\boldsymbol{\sigma}$ is the Newtonian stress tensor, defined in terms of the total fluid velocity as

$$\boldsymbol{\sigma} = -p\mathsf{I} + \eta[\boldsymbol{\nabla}\boldsymbol{u} + (\boldsymbol{\nabla}\boldsymbol{u})^T] \tag{18}$$

where η is the spatially varying viscosity. The term $\phi\boldsymbol{f}_p$ appearing on the right-hand side of Eq. (16) is the body force required to satisfy the rigidity constraint of the particles, the term $\phi\boldsymbol{f}_{sq}$ is the force needed to enforce the "squirming" boundary condition at their surface of the swimmers (Eq. (2)), and final two terms come from the binary-fluid nature of the host fluid.

In the present study, to keep the system as simple as possible, we assume that fluids A and B are strongly immiscible, but otherwise possess identical physical properties, except for their viscosity. Let η_A and η_B represent the viscosity of fluids A and B, respectively, and η_p the viscosity of the particle domains. The total phase-dependent viscosity $\eta(\boldsymbol{r})$ is defined as

$$\begin{aligned}\eta(\boldsymbol{r}) &= \eta_A\psi_A(\boldsymbol{r}) + \eta_B\psi_B(\boldsymbol{r}) + \eta_p\phi(\boldsymbol{r}) \qquad (19)\\ &= \eta_A(\psi_A(\boldsymbol{r}) + \lambda\psi_B(\boldsymbol{r})) + \eta_p\phi(\boldsymbol{r}),\end{aligned}$$

where $\lambda = \eta_B/\eta_A$ is the fluid viscosity ratio. Finally, we have summarized the main symbols and abbreviations used throughout in TableI.

III. RESULTS

In this study, we conducted three-dimensional direct numerical simulations (DNS) of a single particle near an A/B fluid-fluid interface, for a buoyancy-free system in the absence of any externally imposed flow field. In all cases, we use a rectangular simulation box of dimensions $(l_x, l_y, l_z) = (32\Delta, 32\Delta, 64\Delta)$, where Δ is the grid spacing and the unit of length. Periodic boundary conditions are established in all directions. The radius of the squirmer is set to $a = 4\Delta$. For validation, we have also performed simulations at twice the resolution, for the case of $\lambda = 1$, and obtained essentially the same particle trajectories, as shown in Fig. 2. The parameter B_1 in Eq. (2) is set to 0.015, corresponding to a single-particle steady-state velocity of $U_0 = 2/3B_1 = 0.01$. The mobility κ (Eq. (11)), and the mass densities for both fluids and particles $\rho = \rho_A = \rho_B = \rho_p$ are all set to 1. We set the viscosity of the particle and fluid A to be equal to unity, $\eta_p = \eta_A = 1$, and vary the viscosity of fluid B in the range $1/10 \leq \eta_B \leq 10$. Then, the particle Reynolds number is $Re = \rho U_0 a/\eta$ is 0.08 in fluid A, while in fluid B it can range from 0.008 to 0.8. The thermal energy $k_B T$ and reference unit volume v_0 in Eq. (12) are both set to unity. The Péclet number (Pe) is therefore $\mathrm{Pe} = \tau_0/\tau_\kappa = 400$ ($\tau_0 = a/U_0$, $\tau_\kappa = \rho\kappa$), the Schmidt number (Sc) $\mathrm{Sc} = \mathrm{Pe}/\mathrm{Re}$ ranges from 500 to 50000, and the Weber Number is $We = \rho {U_0}^2 a/\sigma_0 = 0.0001$, where $\sigma_0 = \frac{1}{2}(\sigma_{xx} + \sigma_{yy} - 2\sigma_{zz})$ is the surface tension. For this range of parameters, we are working in the limit of high surface tension, where the deformation of the interface is negligible and occurs over time-scales τ_κ that are much smaller than the characteristic particle time-scale τ_0. The fluid-fluid interface thickness ξ_f is of order unity with the present choice of parameter $\alpha = 1$ in Eq. (12), and the particle–fluid interface thickness ξ_p is set to 2.

A schematic representation of our system is given in Fig. 1(a), which shows a single swimmer near a fluid-fluid interface. The system is initialized to be phase separated along the z direction. The swimmer is initially located in Fluid A (the host fluid). The distance between the centre of mass of the swimmer and the interface is L, with $L_{t=0}/a = -4$ unless noted otherwise. This initial distance from the interface is large enough to allow the particle to attain its steady-state

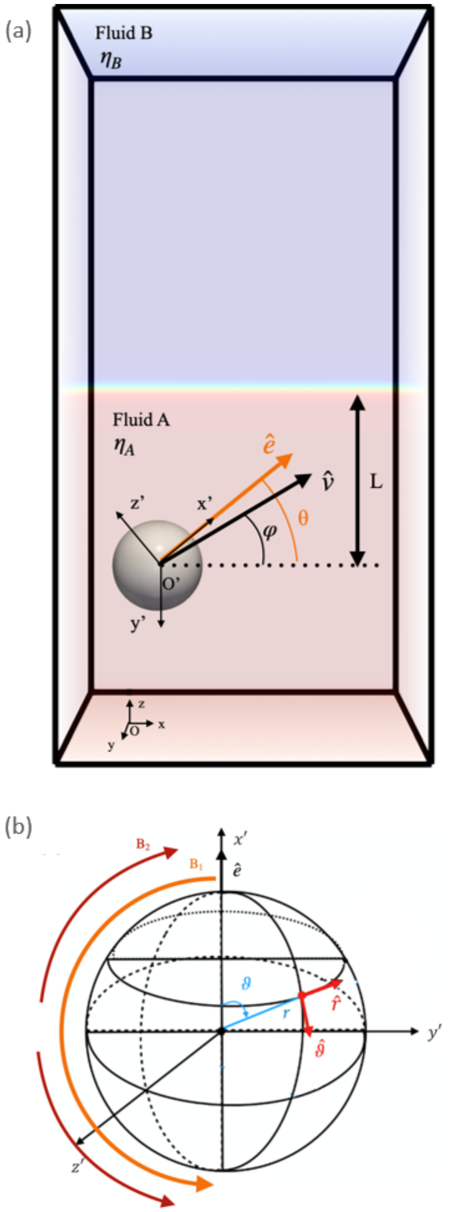

FIG. 1: (a) Schematic representation of a single swimmer near an A/B fluid-fluid interface normal to $\hat{z}$. The angles θ and φ are here the angles between the polar axis and the interface, and the direction of motion and the interface, respectively. (b) Schematic for the squirmer model, with swimming axis $\hat{e}$. The (tangential) surface slip velocity $\boldsymbol{u}^s(\vartheta)$ depends only on the polar angle ϑ, defined as the angle between $\hat{e}$ and the point on the surface at direction $\hat{\boldsymbol{r}}$, with $\hat{\boldsymbol{\vartheta}}$ the unit tangential vector defining the direction of the flow. The B_1 mode ($\propto \sin\vartheta$) will determine the swimming velocity, while the B_2 mode ($\propto \sin 2\vartheta$) gives the stress exerted on the fluid. Here we represent a pusher, generating an extensile flow, as indicated by the negative value of B_2.

velocity before any appreciable particle/interface interactions are observed. The orientation of the interface is specified by its normal vector, $\hat{\boldsymbol{z}}$, that of the swimmer's motion by its normalized velocity vector $\hat{\boldsymbol{v}} = \boldsymbol{V}/|\boldsymbol{V}|$, which need not correspond to its polar axis $\hat{e}$ taken to be parallel to the body frame $\hat{\boldsymbol{x}}'$-axis. The initial orientation of the particle is fixed to lie in the $x-z$ plane, which will constrain its motion to this plane (i.e., $V_y = 0$). The x-component of the position is R_x. The orientation angle $\theta = \arcsin(\hat{\boldsymbol{z}} \cdot \hat{\boldsymbol{e}})$ is defined as the angle between the polar axis and the interface, while the direction of motion is defined by $\varphi = \arcsin(\hat{\boldsymbol{z}} \cdot \hat{\boldsymbol{v}})$.

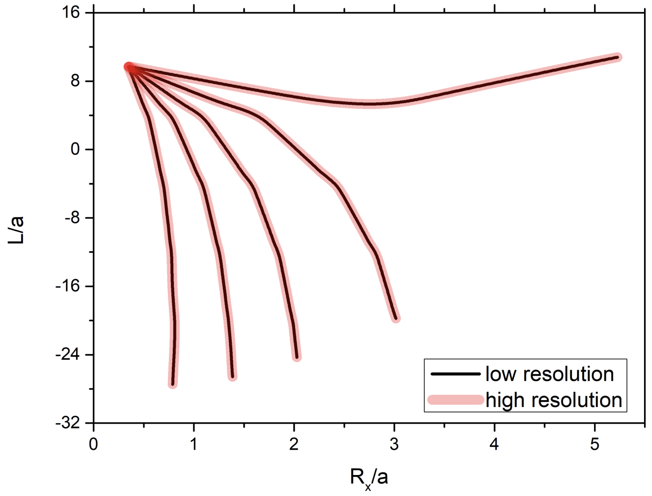

FIG. 2: Particle trajectories for pushers ($\beta = 1$) approaching the interface, with $\lambda = 1$, for two different resolutions. The high-resolution data is drawn in (thick) red lines, whereas the base resolution data used throughout the manuscript is drawn in (thin) black lines.

To understand the dynamics of a swimmer near an interface for fluids with mismatched viscosities, we conduct a series of simulations in which the swimmer is initially in host fluid A, approaches the interface at an incoming angle θ_{in}, and exits this "collision" with an outgoing angle θ_{out}. Given the geometry of our setup, we can focus only on collisions with $\theta_{in} > 0$ (i.e., the swimmer collides with the top interface), as those for $\theta_{in} < 0$ are equivalent due to the reflection symmetry. We consider various initial angles θ_{in} and swimming parameters β, together with a variety of different viscosity ratios $\lambda = 0.1$, 0.2, 1, 5, and 10, in order to construct a phase diagram for the four distinct dynamical modes that result: (i) "penetrating", (ii) "sliding", (iii) "bouncing" and (iv) "hovering", as illustrated in Fig. 3(a). The first three of these modes are also observed in the case of isoviscous fluids ($\lambda = 1$), as reported in our previous work[28]. In case (i), the swimmer crosses the interfacial region separating the fluids, swimming into fluid B with $\theta_{out} > 0$ (see Fig. 4(a)(Multimedia view)). In case (ii), the swimmer becomes trapped at the interface, swimming in the $x-y$ plane with $\theta_{out} = 0$ (see Fig. 4(b)(Multimedia view)). In case (iii), the swimmer approaches the interface and exhibits a significant rotation within the interfacial domain, bouncing back into the host fluid A and avoiding fluid B, leaving the interface with $\theta_{out} < 0$ (see Fig. 4(c)(Multimedia view)). In case (iv), which

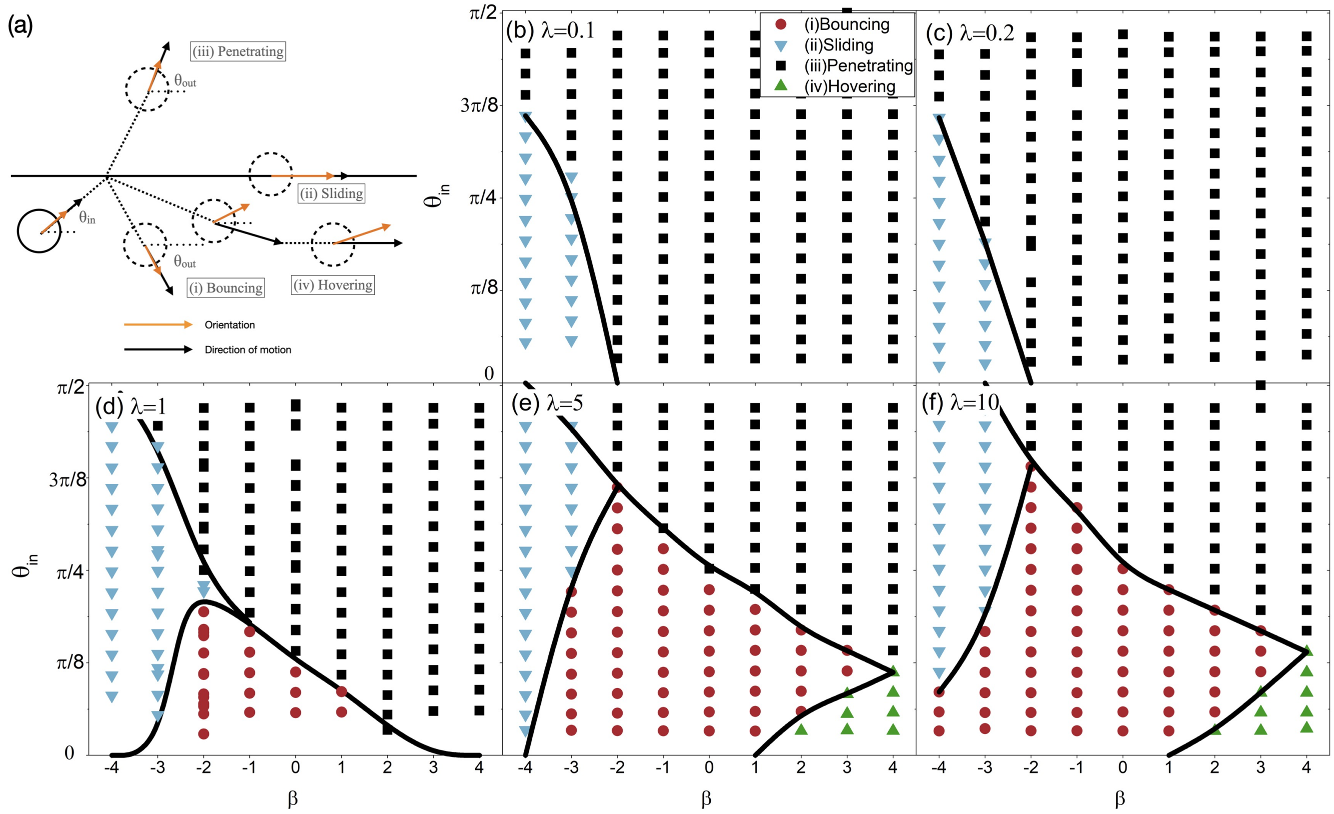

FIG. 3: (a) Graphical illustration of the four collision modes of a swimmer with an interface. Black arrows indicate the swimmer's direction of motion, yellow arrows the swimmer's orientation; (b)–(f) Diagram showing how these modes depend on the initial incidence angle θ_{in} and swimmer type β for various viscosity ratios (b) $\lambda = 0.1$, (c) $\lambda = 0.2$, (d) $\lambda = 1$, (e) $\lambda = 5$, and (f) $\lambda = 10$.

is only observed for $\lambda \neq 0$, the swimmer direction of motion shows characteristic oscillations as it approaches and turns away from the interface, before eventually swimming parallel to the interface at a fixed distance greater than the particle radius $|L| > a$ (see Fig. 4(d)(Multimedia view)). Unlike for the bouncing motion, where the swimmer is able to reorient and swim away from the interface with $\theta < 0$, in the hovering motion the swimmer exhibits a partial reorientation to smaller angles, but it is always pointing towards the interface $\theta > 0$. At the steady state, the self-propulsion will balance with the hydrodynamic interactions with the interface, allowing the swimmer to propel itself parallel to the interface, even though the orientation of the swimmer is not aligned with it. Our results are summarized in the phase diagram of Fig. 3(b)–(f).

In our previous work on isoviscous systems, we have investigated how the collision dynamics depend on the angle of approach θ_{in} and the swimming mode β. For weak swimmers, we observed either penetrating or bouncing motion, depending on the initial orientation: penetration (bouncing) for large (small) angle magnitudes. The bouncing motion is more prevalent for pushers ($\beta < 0$) than pullers ($\beta > 0$), with the latter able to penetrate the interface at smaller angles. Strong pushers usually slide on the interface. The main role of the swimming mode β is to shift the boundary between penetrating and bouncing domains. These results are summarized in Fig. 3(d).

In the case of mismatched viscosities, the focus of the current work, we found that the viscosity ratio λ has a significant effect on the swimmer's motion, as can be seen in Fig. 3. For viscosity ratios less than unity $\lambda < 1$, corresponding to swimmers starting in the high viscosity fluid, the bouncing mode is never observed, rather the penetrating mode dominates for all but the strongest pushers. For such strong pushers, the sliding state can also be observed at small to moderate incoming angles. Fig. 3(b)-(c) shows the results for $\lambda = 0.1$ and 0.2. For viscosity ratios larger than unity $\lambda > 1$, corresponding to a swimmer starting in the lower viscosity fluid, the bouncing mode dominates. Thus, we infer that the viscosity gradient will tend to propel swimmers towards regions of low viscosity and, the swimmers will exhibit a form of viscotaxis, with a preference for the low-viscosity fluid. Finally, for strong pullers at small initial angles, a new dynamical "hovering" mode emerges, while strong pushers still exhibit sliding motion. These results are summarized in Fig. 3(e)-(f), for $\lambda = 5$ and 10.

We further investigate the effect of the viscosity ratio λ on the swimmers' collision dynamics, by computing the map f relating the initial angle θ_{in} to the outgoing angle θ_{out}, after a single collision with the interface. These collision maps are

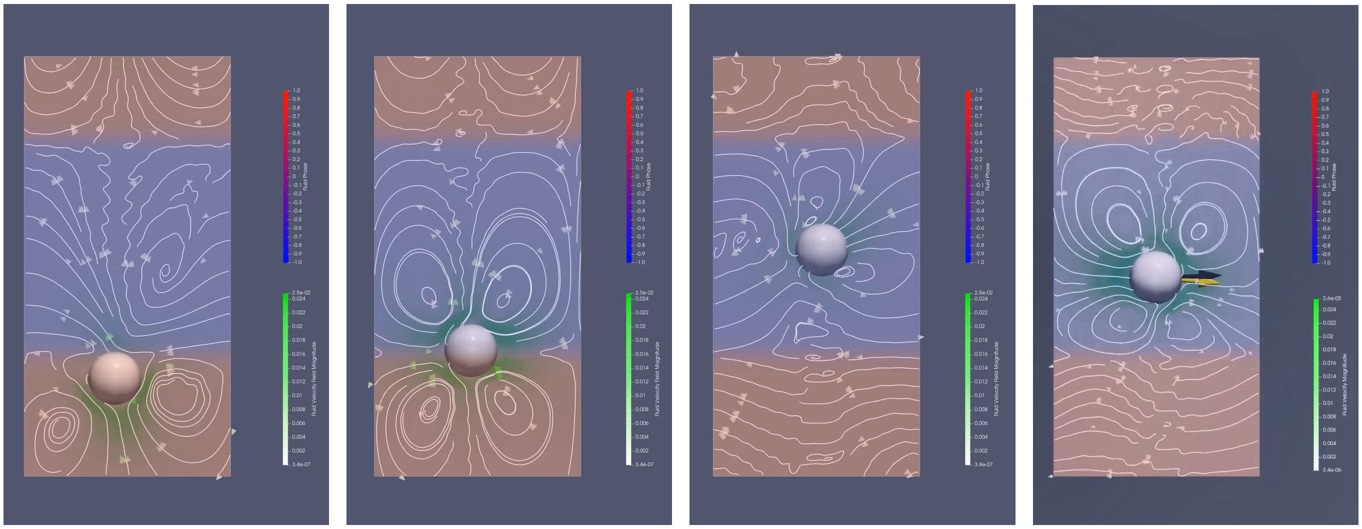

(a) Penetrating $\beta = 3, \theta = \pi/6, \lambda = 1$

(b) Sliding $\beta = -4, \theta = \pi/6, \lambda = 1$

(c) Bouncing $\beta = -1, \theta = \pi/6, \lambda = 5$

(d) Hovering $\beta = 4, \theta = 2\pi/9, \lambda = 10$

FIG. 4: Movies of swimmers displaying the four distinct dynamical modes resulting from collisions with the A/B fluid-fluid interface, including (a) "penetrating" , (b) "sliding", (c) "bouncing" , and (d) "hovering" . In (a), the swimmer crosses the interfacial region, swimming into fluid B with $\theta_{out} > 0$. In (b), the swimmer becomes trapped at the interface with $\theta_{out} = 0$. In (c), the swimmer bounces back into fluid A with $\theta_{out} < 0$. In (d), the swimmer exhibits characteristic oscillations as it approaches and turns away from the interface, before eventually swimming parallel to the interface at a fixed distance, which is greater than the particle radius $|L| > a$. The yellow arrow indicates the particle's squirming direction, while the grey arrow indicates the actual direction of motion. The red/blue colour map represents the fluid A/B order parameter ψ, and the green colour map indicates the magnitude of the fluid velocity. (Multimedia view).

presented in Fig. 5, for $\beta = -2, 0, 2$ swimmers and viscosity ratios $\lambda = 0.2, 1, 5$. Except for the bouncing motion of the neutral particles, which is absent for $\lambda = 0.2$ and extends over a wider range of incoming angles for $\lambda = 5$, the maps for $\lambda \neq 1$ exhibit clear deviations compared to the isoviscous results ($\lambda = 1$). To illustrate this, consider the effect of λ on the collision dynamics of pushers ($\beta = -2$). Compared with the isoviscous system, shown in Fig. 5(d), the minimum angle for penetrating motion $|\theta_{p|min}|$ shifts to larger values when the swimmer is initially in the low-viscosity fluid (i.e., $\lambda = 5$), as shown in Fig. 5(g). Furthermore, the outgoing angle θ_{out} for the penetrating/bouncing motion shows an overall decrease or increase depending on the viscosity ratio. This effect is particularly obvious for the penetrating motion, where the outgoing angle magnitude will be smaller than for the isoviscous case for the same initial angle θ_{in}. The opposite trends are observed for swimmers initially located in the higher viscosity fluid ($\lambda = 0.2$), as shown in Fig. 5(a).

Similar to the isoviscous case, where the pusher/puller duality is evident in the symmetry of the $\theta_{in} - \theta_{out}$ map and the particle trajectories at equal swimming strength $|\beta|$, the results for mismatched viscosities also show a clear symmetry, despite the strong influence of λ on the motion of the swimmer near the interface. We first focus on the penetrating motion, because this was the mode that most clearly evidenced this symmetry for $\lambda = 1$. For a single penetrating process, the trajectories and angular changes mirror each other. To illustrate this, we compare the map $f : \theta_{in} \rightarrow \theta_{out}$ for swimmers with $\beta = \pm 2$, as shown in Fig. 6(a). The mapping for the penetrating motion f_p is symmetric about diagonal $\theta_{out} = \theta_{in}$. That is, the mapping for the pusher is the inverse of the mapping for the corresponding puller, under an inversion of the viscosity ratio, such that $f_p|_{\beta=-2,\lambda=1/5} = f_p^{-1}|_{\beta=2,\lambda=5}$. The minimum angle for penetrating motion $|\theta_{p|min}|$ is equal to the maximum outgoing angle for the puller. To illustrate this, we consider pushers ($\beta = -2$) with $\theta_{in} = 7\pi/18$ at $\lambda = 5$, and pullers ($\beta = 2$) with $\theta_{in} = 11\pi/36$ at $\lambda = 0.2$ as representative examples. Both swimmers are initially set at $L_{t=0} = -4a$. According to Fig. 6(b), the trajectory of the puller (pusher) before it reaches the interface $L < 0$, is the same as the trajectory of the pusher (puller) after it leaves the interface $L > 0$. As expected, this symmetry is also evident in the evolution of the orientation angle, as shown in Fig. 6(c). This behaviour is seen for all swimmer types. In summary, the penetrating motion for pushers (pullers) at viscosity ratio λ, is the inverse of the penetrating motion for pullers (pushers) at viscosity ratio $1/\lambda$, such that $f_p|_{\beta,\lambda} = f_p^{-1}|_{-\beta,1/\lambda}$. When $\lambda = 1$, we recover the results of our previous work, $f_p|_{\beta,\lambda=1} = f_p^{-1}|_{-\beta,\lambda=1}$[28].

We now consider the bouncing motion of pushers and pullers. In view of the observations that a wide variety of swimmer orientations will result in penetration of the interface when the swimmers are moving into the low-viscosity fluid ($\lambda < 1$) and that the pullers tend to penetrate at $\lambda = 1$, we will focus on $\lambda > 1$. According to Fig. 7(a), the mapping for the bouncing motion f_b of swimmers $\beta = \pm 2$ at a high viscosity interface ($\lambda = 5$) is symmetric about the diagonal

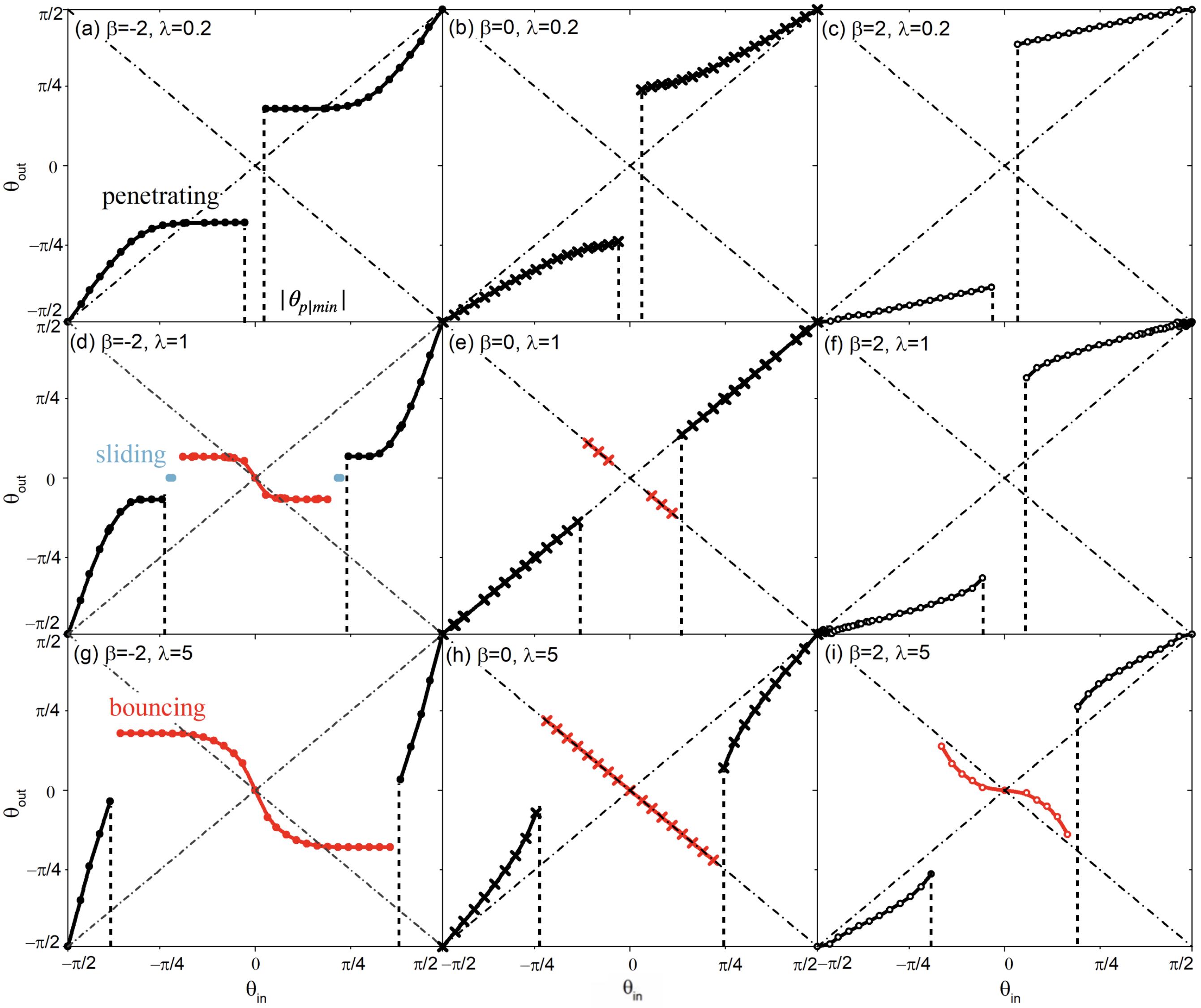

FIG. 5: Changes in the orientation angle θ for different viscosity ratios (a)-(c) $\lambda = 0.2$; (d)-(f) $\lambda = 1$; (g)-(i) $\lambda = 5$ with swimmers with various swimming types $\beta = -2$, 0 and 2 after a single collision with the interface. This corresponds to a one-to-one mapping from θ_{in} to θ_{out}. The vertical dashed lines mark the edge of the penetrating region, indicating the value of $\theta_{p|min}$.

$\theta_{out} = -\theta_{in}$. Thus, the pusher/puller duality can be expressed as $f_b|_{\beta,\lambda} = -f_b^{-1}|_{-\beta,\lambda}$. This can be seen by comparing the results obtained from simulations of a single bouncing process, i.e. a pusher ($\beta = -2$) with $\theta_{in} = -\pi/6$ and a puller ($\beta = 2$) with $\theta_{in} = -5\pi/18$, both under $\lambda = 5$. The time-evolution of the particle positions and orientations for this process are shown in Fig. 7(b-c). The pusher/puller trajectories are mirror images of each other, resulting from the time reversibility at a low Reynolds number. That is, the trajectory for the bouncing motion of a pusher (puller) corresponds to the (time-reversed) bouncing motion of a puller (pusher).

The bouncing motion for neutral particles, corresponding to the red curves in Fig. 5(e) and (h), is particularly interesting in how insensitive it is to λ, in contrast to pusher/pullers. Even though $|\theta_{p|min}|$ is seen to increase upon increasing λ, the outgoing angle θ_{out} is always equal in magnitude to the approaching angle θ_{in}, regardless of the viscosity ratio λ. This represents a special case of the bouncing map obtained for pushers/pullers, $f_b|_{\beta,\lambda} = -f_b^{-1}|_{-\beta,\lambda}$, with $\beta = 0$. In order to further validate this observation, we conducted a series of simulations for neutral particles with various fluid viscosity ratios $\lambda = 1$, 5, and 10. The particles initially approach the interface with $\theta_{in} = \pi/12$. The effect of the viscosity is evident in the distance of the shortest approach to the interface $|L^b_{min}|$, which decreases with decreasing λ, as shown in Fig. 8(a). Although the collision time shows little dependence on the viscosity ratio (Fig. 8(b)), the distance of closest approach is very sensitive to the viscosity ratio, with a larger difference resulting in

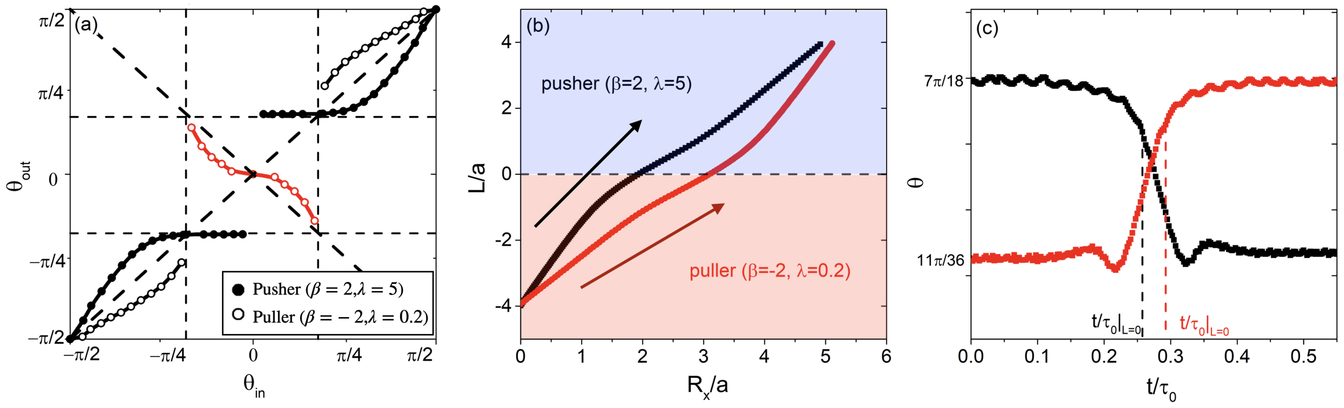

FIG. 6: (a) Collisions maps, providing the change in the orientation angle θ for a puller ($\beta = 2$) at $\lambda = 5$ and a pusher ($\beta = -2$) at $\lambda = 1/5$, marked by empty and filled circles, respectively. The black symbols represent the penetrating motion, red symbols the bouncing motion. (b) The particle trajectory and (c) the time evolution of the orientation angle θ, for swimmers initially located at $L_{t=0} = -4a$. The pusher with $\beta = -2$, $\theta_{in} = 7\pi/18$, and $\lambda = 5$ is marked in black, while the puller with $\beta = 2$, $\theta_{in} = 11\pi/36$, and $\lambda = 1/5$ is marked in red.

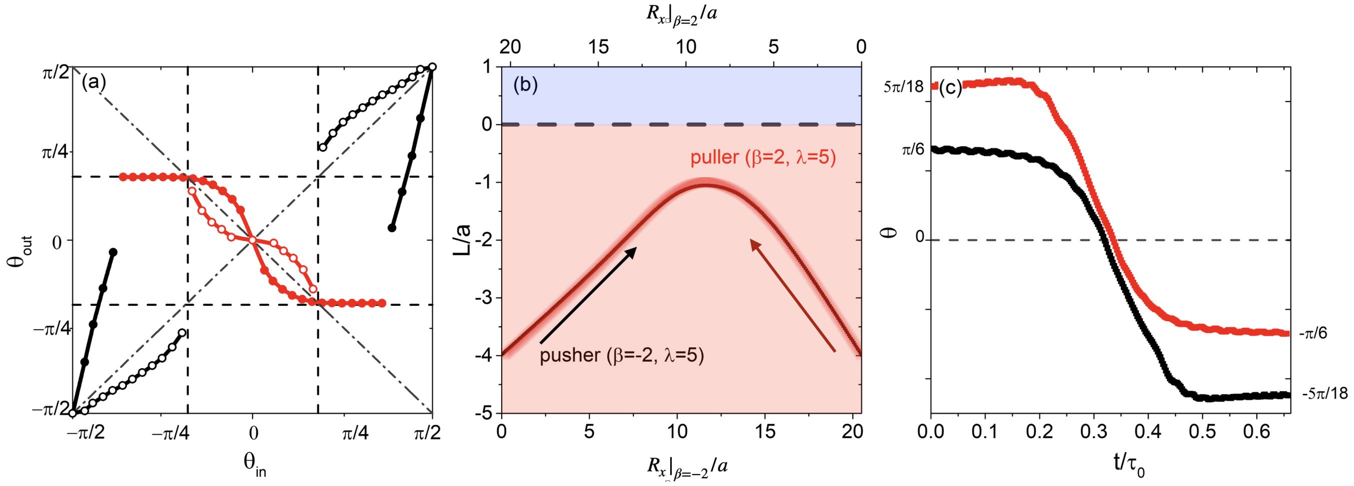

FIG. 7: (a) Collision maps, providing the change in the orientation angle θ for a puller ($\beta = 2$) and a pusher ($\beta = -2$) at $\lambda = 5$, marked by empty and filled circles respectively, (b) the particle trajectory and (c) the time evolution of the orientation angle θ for swimmers initially located at $L_{t=0} = -4a$. The pusher ($\beta = -2$) with $\theta_{in} = \pi/6$ is marked in black, while the puller ($\beta = 2$) with $\theta_{in} = 5\pi/18$ is marked in red.

longer-range interactions, which allow the particle to start its reorientation process to escape the interface earlier.

Finally, for strong pullers, we have observed a new "hovering" mode, different from the penetrating, bouncing, or sliding motions. To study this motion, we conducted simulations for a puller with $\beta = 4$, at various approaching angles $\theta_{in} = \pi/9$, $\pi/12$, $\pi/18$ and $\pi/36$, with the particle initially located at $L_{t=0} = -4a$. The swimmer approaches the interface, initially turning towards it while showing oscillations in its direction of motion. The swimmer then partially turns away from the interface, with increased oscillations in its orientation, before settling into the hovering motion, moving parallel to the interface at a fixed distance (see Fig. 9(a)). We note that the orientation of the swimmer is not completely aligned with the interface, it is always pointing towards the interface, with a positive θ throughout the entire process, as shown in Fig. 9(b). Taking the dynamics of a $\beta = 4$ puller, with initial angle $\theta_{in} = \pi/9$, for $\lambda = 10$ as a reference (see Fig. 9(c)), we can clearly see that the orientation of the swimmer and its direction of motion are not parallel. In contrast to these pullers, strong pushers will show a sliding motion, in which they are adsorbed to and swim along the interface[28].

IV. DISCUSSION

We have studied the effect of a viscosity ratio in a binary phase-separated fluid on the dynamics of swimmers near the interface. We notice that swimmers show a preference towards the lower viscosity fluid. If one considers an ensem-

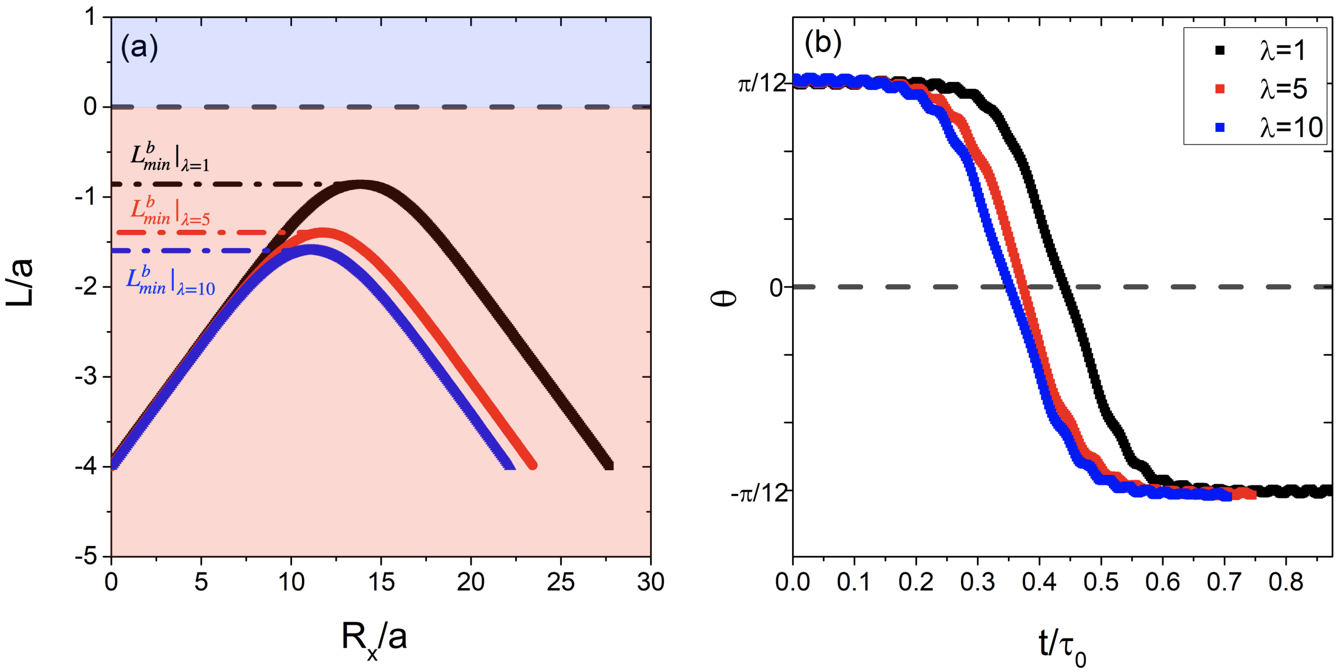

FIG. 8: (a) The particle trajectory and (b) the time evolution of the orientation angle θ, for neutral particles ($\beta = 0$) at $\lambda = 1$, 5 and 10. All swimmers are initially located at $L_{t=0} = -4a$, with orientation $\theta_{in} = \pi/12$.

ble of swimmers, with a variety of incidence angles, the effect of the viscosity gradient will be to propel swimmers towards regions of low viscosity. This will tend to result in an enrichment of swimmers in the low-viscosity fluid. This type of viscotaxis is consistent with previous theoretical investigations on swimmers in viscosity gradients.[26,46–49] These studies showed that a squirmer in a weak viscosity gradient will reorient in the direction of the lower viscosity region (negative viscotaxis), regardless of the swimming mode. This effect has been confirmed in experiments, such as the puller-like alga *Chlamydomonas reinhardtii*, which was observed to accumulate in low-viscosity zones at sufficiently strong gradients[50–54].

We observe a new mode of motion for strong pullers which we refer to as hovering. This mode was not observed for swimmers in fluids of equal viscosity. A similar mode has been reported in previous work that focused on pullers near a wall, rather than a deformable fluid-fluid interface at finite λ[10–14]. Although it is difficult to make a direct comparison with our work, the dynamics previously reported for pullers near rigid walls is similar to the hovering motion we observe. In both their work and ours, strong pullers first exhibit oscillating motion before eventually swimming parallel to the interface at a constant separation, maintaining an orientation tilted towards the interface (i.e., the particle orientation is not aligned with the direction of motion). Some understanding of this similarity can be obtained by noting that a solid wall can be regarded as a fluid-fluid interface in the limit $\lambda \to \infty$. Furthermore, for the hovering motion, the swimmers remain in the host (low viscosity) fluid, with the distance of the closest approach increasing as the viscosity ratio λ increases. Thus, the interaction with the interface can be expected to be well represented by the far-field approximations used in previous studies[12]. Finally, in order to rule out the possibility that the observed dynamics are due to inertial effects, we also conducted simulations with a smaller Reynolds number by decreasing the velocity of swimmers. We obtained equivalent trajectories, which indicates that the inertial effects are negligible in our present simulations.

V. CONCLUSIONS

In this work, we have analyzed the dynamics of swimmers approaching a fluid-fluid interface between phase-separated fluids with distinct viscosities. The viscosity ratio λ, together with the swimming mode β (pusher or puller), determine the outcome of collisions of the swimmer with the interface. Such collisions are shown to give rise to four distinct dynamic modes: bouncing, sliding, penetrating and hovering. Compared with the results obtained for isoviscous systems $\lambda = 1$, we observe that the swimmer exhibits a preference towards the lower viscosity fluid (i.e. viscotaxis). This preference should be understood in the sense that, for a wide distribution of contact angles, more swimmers will transition into the low viscous environment than vice-versa. This means that a typical swimmer, drawn from this distribution, that starts in a low viscosity fluid is more likely to bounce back (reflect) at the interface, while a swimmer starting in the high viscosity fluid is more likely to penetrate the interface and swim into the lower viscosity fluid. Even though the outgoing angle θ_{out} for the penetrating/bouncing motion is mainly determined by the

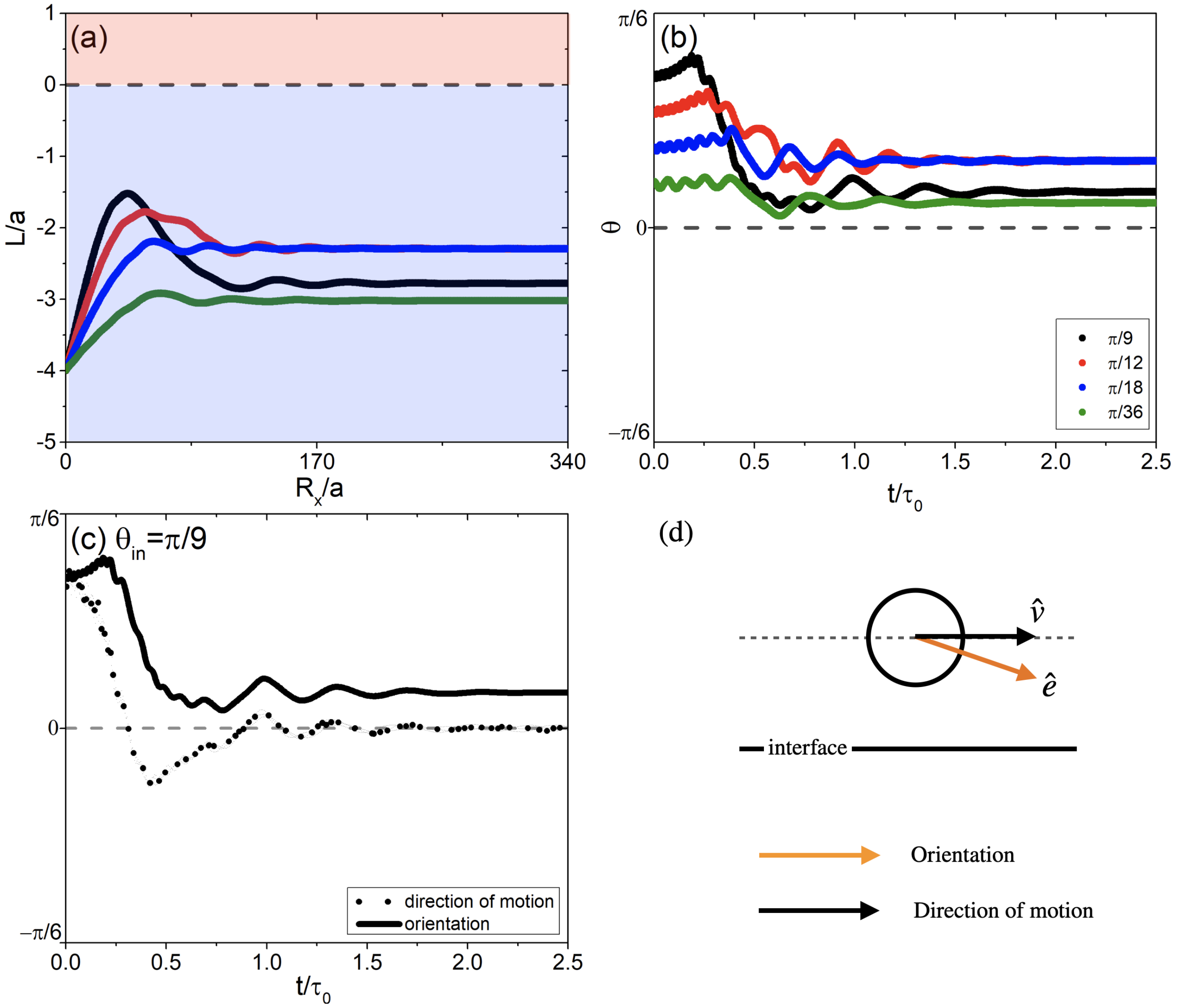

FIG. 9: The new dynamical mode of "hovering motion" results in particles swimming in the low-viscosity fluid parallel to the interface without touching it. (a) The particle trajectories as well as (b) the time evolution of the orientation angle θ for pullers ($\beta = 4$) at $\lambda = 10$, for various approach orientations θ_{in}, with the swimmers initially located at $L_{t=0} = -4a$; (c) Shows the time evolution for θ (solid line) and φ (dotted line), i.e., the orientation and direction of motion, respectively, for a puller ($\beta = 4$) at $\lambda = 10$, with $\theta_{in} = \pi/9$. (d) Graphical illustration of the swimming state for a strong puller in a typical hovering motion.

swimming type β and the initial angle θ_{in}, the precise functional dependence depends on the viscosity ratio λ. A duality between pushers/pullers can be clearly seen in the trajectories for penetrating and bouncing swimmers. In addition, we observed that strong pullers, initially located in the lower viscosity fluid, can exhibit a new type of hovering motion, moving parallel to the interface at a fixed distance $L/a > 1$, which is not observed for isoviscous systems.

Our study represents a detailed analysis of the role played by the viscosity ratio on the dynamics of swimmers near an interface. This improves our understanding of swimming in complex fluid environments and may help with the interpretation of similar physiological and biological phenomena. Future work will explore the role of surface tension and curvature, as well as allow for non-Newtonian host fluids, which are more representative of biological environments. We also aim to examine more complex chemical interactions, in particular for the particle-fluid and particle-interface interactions. Furthermore, it is also important to consider the possible deformations of microorganisms as they cross the liquid-liquid interface. By addressing these limitations and developing more realistic models, we will be ale to better understand the complexities of micro-swimmer dynamics at interfaces, with the hope of contributing to the development of advanced artificial micro-swimmers.

ACKNOWLEDGMENTS

The authors express their gratitude to Dr. Hiroto Ozaki and Dr. Takeshi Aoyagi for their collaboration and outstanding contributions to the simulation software development. R.Y. acknowledges helpful discussions with Profs. Hajime Tanaka and Akira Furukawa. This work was supported by the Grants-in-Aid for Scientific Research (JSPS KAKENHI) under grant nos. JP 20H00129, 20H05619, and 20K03786 and by the NEDO Project (JPNP16010). This work was supported by JST, the establishment of university fellowships towards the creation of science technology innovation, Grant Number JPMJFS2123.

DATA AVAILABILITY

The data that support the findings of this study are available from the corresponding author upon reasonable request.

Appendix A: Software

All simulations presented in this paper were conducted using the open-source version of the KAPSEL DNS software. KAPSEL has been developed in our lab to simulate the dynamics of solid particles dispersed in complex fluids. Detailed descriptions of KAPSEL are available online (https://kapsel-dns.com).

Appendix B: Computational Algorithm

In this appendix, we briefly describe the fractional step approach used to solve for the coupled fluid/particle dynamics. Time step n is given by $t_n = nh$, with h the time interval. First, the total velocity field is updated with the advection and viscous stress contributions. Simultaneously, we update the particle positions and orientations,

$$\begin{aligned}
\boldsymbol{u}^* &= \boldsymbol{u}^n + \int_{t_n}^{t_n+h} \mathrm{d}s \nabla \cdot \left[\frac{1}{\rho}(-p^* \boldsymbol{I} + \boldsymbol{\sigma}) - \boldsymbol{u}\boldsymbol{u}\right] \\
\boldsymbol{R}_i^{n+1} &= \boldsymbol{R}_i^n + \int_{t_n}^{t_n+h} \mathrm{d}s \boldsymbol{V}_i \\
\boldsymbol{Q}_i^{n+1} &= \boldsymbol{Q}_i^n + \int_{t_n}^{t_n+h} \mathrm{d}s \boldsymbol{Q}_i \cdot \mathrm{skew}(\Omega_i)
\end{aligned}$$

with $p^\star$ computed to ensure the divergence-free condition of this updated velocity field, $\nabla \cdot \boldsymbol{u}^* = 0$.

Second, the time-integrated hydrodynamic force and torque are obtained from the momentum exchange over the particle domain,

$$\begin{aligned}
\int_{t_n}^{t_n+h} \mathrm{d}s \boldsymbol{F}_i^H &\simeq h\boldsymbol{F}_i^H = \int \mathrm{d}\boldsymbol{x} \rho \phi_i^{n+1} (\boldsymbol{u}^* - \boldsymbol{u}_p^n) \\
\int_{t_n}^{t_n+h} \mathrm{d}s \boldsymbol{N}_i^H &\simeq h\boldsymbol{N}_i^H = \int \mathrm{d}\boldsymbol{x} [\boldsymbol{r}_i^{n+1} \times \rho \phi_i^{n+1} (\boldsymbol{u}^* - \boldsymbol{u}_p^n)]
\end{aligned}$$

Based on this, and the remaining forces acting on the colloids, the particle velocities are updated as

$$\begin{aligned}
\boldsymbol{V}_i^{n+1} &= \boldsymbol{V}_i^n + M_p^{-1}\left[\int_{t_n}^{t_n+h} \mathrm{d}s \boldsymbol{F}_i^H\right] \\
&\quad + M_p^{-1}\left[\int_{t_n}^{t_n+h} \mathrm{d}s (\boldsymbol{F}_i^C + \boldsymbol{F}^e xt_i)\right] \\
\boldsymbol{\Omega}_i^{n+1} &= \boldsymbol{\Omega}_i^n + \boldsymbol{I}_p^{-1}\left[\int_{t_n}^{t_n+h} \mathrm{d}s \boldsymbol{N}_i^H\right] \\
&\quad + \boldsymbol{I}_p^{-1}\left[\int_{t_n}^{t_n+h} \mathrm{d}s \boldsymbol{N}^e xt_i\right]
\end{aligned}$$

Finally, the velocity field is updated to include the penalty force $\phi \boldsymbol{f}_p$, which ensures the rigidity constraint, within the particle domain, for the total velocity field,

$$\begin{aligned}
\boldsymbol{u}^{n+1} &= \boldsymbol{u}^n + \left[\int_{t_n}^{t_n+h} \mathrm{d}s \phi \boldsymbol{f}_p\right] \\
\left[\int_{t_n}^{t_n+h} \mathrm{d}s \phi \boldsymbol{f}_p\right] &= \phi^{n+1}(\boldsymbol{u}_p^{n+1} - \boldsymbol{u}^*) - \frac{h}{\rho}\nabla p_p
\end{aligned}$$

where the pressure here comes from the rigidity constraint, and is again obtained from the incompressibility condition $\nabla \cdot \boldsymbol{u}^{n+1} = 0$. The total pressure field is thus $p = p^* + p_p$.

Appendix C: Dimensional analysis

To generalize the solutions, it is convenient to introduce dimensionless variables. Using as basic units the density ρ, particle radius a, and steady-state swimming velocity $U_0 = 2/3B_1$, the derived units for the remaining physical quantities are:

$$\begin{aligned}
[\mathrm{Time}] :& a/U_0 \\
[\mathrm{Mass}] :& \rho a^3 \\
[\mathrm{Force}] :& \rho a^2 U_0^2 \\
[\mathrm{Pressure}] :& \rho U_0^2 \\
[\mathrm{Energy}] :& \rho a^3 U_0^2 \\
[\mathrm{Acceleration}] :& U_0^2/a \\
[\mathrm{Mobility}] :& \frac{a}{\rho U_0}
\end{aligned}$$

The dimensionless form of the Navier-Stokes and Cahn-Hilliard equations is

$$\begin{aligned}
(\partial_t^* + \boldsymbol{u}^* \cdot \boldsymbol{\nabla}^*)\boldsymbol{u}^* &= \boldsymbol{\nabla}^* \cdot \boldsymbol{\sigma}^* + \phi \boldsymbol{f}_p^* + \boldsymbol{f}_{sq}^* - \psi \boldsymbol{\nabla}^* \mu_\psi^* - \phi \boldsymbol{\nabla}^* \mu_\phi^* \\
(\partial_t^\star + \boldsymbol{u}^\star \cdot \boldsymbol{\nabla}^\star)\psi &= \kappa^\star \nabla^{\star 2} \mu_\psi^\star
\end{aligned}$$

where the non-dimensionalized variables are defined as

$$
\begin{aligned}
\boldsymbol{u}^\star &= \frac{1}{U_0}\boldsymbol{u}\\
\partial_t^\star &= \frac{a}{U_0}\partial_t\\
\boldsymbol{\nabla}^\star &= a\boldsymbol{\nabla}\\
p^\star &= \frac{1}{\rho U_0^2}p\\
\boldsymbol{\sigma}^\star &= \frac{1}{\rho U_0^2}\boldsymbol{\sigma} = -p^\star\mathsf{I} + \frac{1}{\mathrm{Re}}\left(\boldsymbol{\nabla}^\star\boldsymbol{u}^\star + (\boldsymbol{\nabla}^\star\boldsymbol{u}^\star)^T\right)\\
\phi\boldsymbol{f}_p^\star &= \frac{a}{U_0^2}\boldsymbol{f}_p\\
\boldsymbol{f}_{sq}^\star &= \frac{a}{U_0^2}\boldsymbol{f}_{sq}\\
\mu_\alpha^\star &= \frac{1}{\rho U_0^2}\mu_\alpha\\
\kappa^\star &= \frac{\rho U_0}{a}\kappa = \frac{1}{\mathrm{Pe}}
\end{aligned}
$$

with the Reynolds and Peclet numbers given by ($\tau_0 = a/U_0$ and $\tau_\kappa = \rho\kappa$)

$$
\begin{aligned}
\mathrm{Re} &= \frac{\rho U_0 a}{\eta}\\
\mathrm{Pe} &= \tau_0/\tau_\kappa
\end{aligned}
$$

[1] J. C. Kirkman-Brown and D. J. Smith, "Sperm motility: is viscosity fundamental to progress?" MHR: Basic science of reproductive medicine **17**, 539–544 (2011).

[2] H. Gadêlha, E. Gaffney, D. Smith, and J. Kirkman-Brown, "Nonlinear instability in flagellar dynamics: a novel modulation mechanism in sperm migration?" Journal of The Royal Society Interface **7**, 1689–1697 (2010).

[3] L. Björndahl, "The usefulness and significance of assessing rapidly progressive spermatozoa," Asian Journal of Andrology **12**, 33 (2010).

[4] H. V. Nguyen and V. Faivre, "Targeted drug delivery therapies inspired by natural taxes," Journal of Controlled Release **322**, 439–456 (2020).

[5] H. Ceylan, I. C. Yasa, O. Yasa, A. F. Tabak, J. Giltinan, and M. Sitti, "3d-printed biodegradable microswimmer for drug delivery and targeted cell labeling," BioRxiv , 379024 (2018).

[6] B. Mostaghaci, O. Yasa, J. Zhuang, and M. Sitti, "Bioadhesive bacterial microswimmers for targeted drug delivery in the urinary and gastrointestinal tracts," Advanced Science **4**, 1700058 (2017).

[7] B.-W. Park, J. Zhuang, O. Yasa, and M. Sitti, "Multifunctional bacteria-driven microswimmers for targeted active drug delivery," ACS nano **11**, 8910–8923 (2017).

[8] X. Yan, Q. Zhou, J. Yu, T. Xu, Y. Deng, T. Tang, Q. Feng, L. Bian, Y. Zhang, A. Ferreira, *et al.*, "Magnetite nanostructured porous hollow helical microswimmers for targeted delivery," Advanced Functional Materials **25**, 5333–5342 (2015).

[9] D. Laage and J. T. Hynes, "A molecular jump mechanism of water reorientation," Science **311**, 832–835 (2006).

[10] K. Ishimoto and E. A. Gaffney, "Squirmer dynamics near a boundary," Physical Review E **88**, 062702 (2013).

[11] J. S. Lintuvuori, A. T. Brown, K. Stratford, and D. Marenduzzo, "Hydrodynamic oscillations and variable swimming speed in squirmers close to repulsive walls," Soft Matter **12**, 7959–7968 (2016).

[12] G.-J. Li and A. M. Ardekani, "Hydrodynamic interaction of microswimmers near a wall," Physical Review E **90**, 013010 (2014).

[13] I. Pagonabarraga and I. Llopis, "The structure and rheology of sheared model swimmer suspensions," Soft Matter **9**, 7174–7184 (2013).

[14] Z. Shen, A. Würger, and J. S. Lintuvuori, "Hydrodynamic interaction of a self-propelling particle with a wall," The European Physical Journal E **41**, 1–9 (2018).

[15] G. Volpe, I. Buttinoni, D. Vogt, H.-J. Kümmerer, and C. Bechinger, "Microswimmers in patterned environments," Soft Matter **7**, 8810–8815 (2011).

[16] F. Fadda, J. J. Molina, and R. Yamamoto, "Dynamics of a chiral swimmer sedimenting on a flat plate," Physical Review E **101**, 052608 (2020).

[17] E. Lauga, W. R. DiLuzio, G. M. Whitesides, and H. A. Stone, "Swimming in circles: motion of bacteria near solid boundaries," Biophysical journal **90**, 400–412 (2006).

[18] P. Malgaretti and J. Harting, "Phoretic colloids close to and trapped at fluid interfaces," ChemNanoMat **7**, 1073–1081 (2021).

[19] T. Peter, P. Malgaretti, N. Rivas, A. Scagliarini, J. Harting, and S. Dietrich, "Numerical simulations of self-diffusiophoretic colloids at fluid interfaces," Soft Matter **16**, 3536–3547 (2020).

[20] R. Di Leonardo, D. Dell'Arciprete, L. Angelani, and V. Iebba, "Swimming with an image," Physical review letters **106**, 038101 (2011).

[21] R. A. Shah, Z. Asghar, and N. Ali, "Mathematical modeling related to bacterial gliding mechanism at low Reynolds number with Ellis Slime," The European Physical Journal Plus **137**, 600 (2022).

[22] Z. Asghar, W. Shatanawi, and S. Hussain, "Biomechanics of bacterial gliding motion with Oldroyd-4 constant slime," The European Physical Journal Special Topics (2022), 10.1140/epjs/s11734-022-00723-2.

[23] Z. Asghar, R. A. Shah, W. Shatanawi, and N. Ali, "FENE-P fluid flow generated by self-propelling bacteria with slip effects," Computers in Biology and Medicine **153**, 106386 (2023).

[24] X. Wang, M. In, C. Blanc, P. Malgaretti, M. Nobili, and A. Stocco, "Wetting and orientation of catalytic janus colloids at the surface of water," Faraday discussions **191**, 305–324 (2016).

[25] P. Malgaretti, M. Popescu, and S. Dietrich, "Self-diffusiophoresis induced by fluid interfaces," Soft Matter **14**, 1375–1388 (2018).

[26] H. Gidituri, Z. Shen, A. Würger, and J. S. Lintuvuori, "Reorientation dynamics of microswimmers at fluid-fluid interfaces," Physical Review Fluids **7**, L042001 (2022).

[27] E. A. Gaffney, H. Gadêlha, D. J. Smith, J. R. Blake, and J. C. Kirkman-Brown, "Mammalian sperm motility: observation and theory," Annual Review of Fluid Mechanics (2011).

[28] C. Feng, J. J. Molina, M. S. Turner, and R. Yamamoto, "Dynamics of microswimmers near a soft penetrable interface," Phys. Rev. Res. **4**, 043202 (2022).

[29] M. J. Lighthill, "On the squirming motion of nearly spherical deformable bodies through liquids at very small reynolds numbers," Communications on Pure and Applied Mathematics **5**, 109–118 (1952), https://onlinelibrary.wiley.com/doi/pdf/10.1002/cpa.3160050201.

[30] M. T. Downton and H. Stark, "Simulation of a model microswimmer," Journal of Physics: Condensed Matter **21**, 204101 (2009).

[31] O. S. Pak and E. Lauga, "Generalized squirming motion of a sphere," Journal of Engineering Mathematics **88**, 1–28 (2014).

[32] T. Ishikawa, M. Simmonds, and T. J. Pedley, "Hydrodynamic interaction of two swimming model micro-organisms," Journal of Fluid Mechanics **568**, 119–160 (2006).

[33] T. J. Pedley, D. R. Brumley, and R. E. Goldstein, "Squirmers with swirl: a model for volvox swimming," Journal of Fluid Mechanics **798**, 165–186 (2016).

[34] H. Shinto, "Computer simulation of wetting, capillary forces, and particle-stabilized emulsions: From molecular-scale to mesoscale modeling," Advanced Powder Technology **23**, 538–547 (2012).

[35] G. Lecrivain, R. Yamamoto, U. Hampel, and T. Taniguchi, "Direct numerical simulation of a particle attachment to an immersed bubble," Physics of Fluids **28**, 083301 (2016).

[36] G. Lecrivain, T. B. P. Grein, R. Yamamoto, U. Hampel, and T. Taniguchi, "Eulerian/lagrangian formulation for the elasto-capillary deformation of a flexible fibre," Journal of Computational Physics **409**, 109324 (2020).

[37] R. Yamamoto, J. J. Molina, and Y. Nakayama, "Smoothed profile method for direct numerical simulations of hydrodynamically interacting particles," Soft Matter **17**, 4226–4253 (2021).

[38] Y. Nakayama and R. Yamamoto, "Simulation method to resolve hydrodynamic interactions in colloidal dispersions," Phys. Rev. E **71**, 036707 (2005).

[39] Y. Nakayama and R. Yamamoto, "Simulation method to resolve hydrodynamic interactions in colloidal dispersions," Phys. Rev. E **71**, 036707 (2005).

[40] J. J. Molina and R. Yamamoto, "Direct numerical simulations of rigid body dispersions. i. mobility/friction tensors of assemblies of spheres," The Journal of chemical physics **139**, 234105 (2013).

[41] K. Kim, Y. Nakayama, and R. Yamamoto, "Direct numerical simulations of electrophoresis of charged colloids," Phys. Rev. Lett. **96**, 208302 (2006).

[42] A. Hamid, J. J. Molina, and R. Yamamoto, "Sedimentation of non-brownian spheres at high volume fractions," Soft Matter **9**, 10056–10068 (2013).

[43] J. J. Molina, K. Otomura, H. Shiba, H. Kobayashi, M. Sano, and R. Yamamoto, "Rheological evaluation of colloidal dispersions using the smoothed profile method: Formulation and applications," Journal of Fluid Mechanics **792**, 590–619 (2016).

[44] J. J. Molina, Y. Nakayama, and R. Yamamoto, "Hydrodynamic interactions of self-propelled swimmers," Soft Matter **9**, 4923–4936 (2013).

[45] X. Luo, M. R. Maxey, and G. E. Karniadakis, "Smoothed profile method for particulate flows: Error analysis and simulations," Journal of Computational Physics **228**, 1750–1769 (2009).

[46] C. Datt and G. J. Elfring, "Active particles in viscosity gradients," Physical Review Letters **123**, 158006 (2019).

[47] B. Liebchen, P. Monderkamp, B. Ten Hagen, and H. Löwen, "Viscotaxis: Microswimmer navigation in viscosity gradients," Physical review letters **120**, 208002 (2018).

[48] R. Dandekar and A. M. Ardekani, "Swimming sheet in a viscosity-stratified fluid," Journal of Fluid Mechanics **895** (2020).

[49] P. S. Eastham and K. Shoele, "Axisymmetric squirmers in stokes fluid with nonuniform viscosity," Physical Review Fluids **5**, 063102 (2020).

[50] M. J. Daniels, J. M. Longland, and J. Gilbart, "Aspects of motility and chemotaxis in spiroplasmas," Microbiology **118**, 429–436 (1980).

[51] K. Takabe, H. Tahara, M. S. Islam, S. Affroze, S. Kudo, and S. Nakamura, "Viscosity-dependent variations in the cell shape and swimming manner of leptospira," Microbiology **163**, 153–160 (2017).

[52] S. Coppola and V. Kantsler, "Green algae scatter off sharp viscosity gradients," Scientific reports **11**, 1–7 (2021).

[53] M. R. Stehnach, N. Waisbord, D. M. Walkama, and J. S. Guasto, "Viscophobic turning dictates microalgae transport in viscosity gradients," Nature Physics **17**, 926–930 (2021).

[54] C. E. López, J. Gonzalez-Gutierrez, F. Solorio-Ordaz, E. Lauga, and R. Zenit, "Dynamics of a helical swimmer crossing viscosity gradients," Physical Review Fluids **6**, 083102 (2021).